ACS APPLIED MATERIALS & INTERFACES

Research Article

Cite This: ACS Appl. Mater. Interfaces 2019, 11, 15913−15921

www.acsami.org

Oxygen-Induced In Situ Manipulation of the Interlayer Coupling and Exciton Recombination in Bi_2Se_3/MoS_2 2D Heterostructures

Zachariah Hennighausen,[†] Christopher Lane,[†] Abdelkrim Benabbas,[‡] Kevin Mendez,[†] Monika Eggenberger,[†] Paul M. Champion,[‡] Jeremy T. Robinson,[§] Arun Bansil,[‡] and Swastik Kar*[,†]

[†]Department of Physics and [‡]Physics Department and Center for Interdisciplinary Research on Complex Systems, Northeastern University, Boston, Massachusetts 02115, United States

[§]Naval Research Laboratory, Washington, District of Columbia 20375, United States

Supporting Information

ABSTRACT: Two-dimensional (2D) heterostructures are more than a sum of the parent 2D materials, but are also a product of the interlayer coupling, which can induce new properties. In this paper, we present a method to tune the interlayer coupling in Bi_2Se_3/MoS_2 2D heterostructures by regulating the oxygen presence in the atmosphere, while applying laser or thermal energy. Our data suggest that the interlayer coupling is tuned through the diffusive intercalation and deintercalation of oxygen molecules. When one layer of Bi_2Se_3 is grown on monolayer MoS_2, an influential interlayer coupling is formed, which quenches the signature photoluminescence (PL) peaks. However, thermally treating in the presence of oxygen disrupts the interlayer coupling, facilitating the emergence of the MoS_2 PL peak. Our density functional theory calculations predict that intercalated oxygen increases the interlayer separation ∼17%, disrupting the interlayer coupling and inducing the layers to behave more electronically independent. The interlayer coupling can then be restored by thermally treating in N_2 or Ar, where the peaks will requench. Hence, this is an interesting oxygen-induced switching between "non-radiative" and "radiative" exciton recombination. This switching can also be accomplished locally, controllably, and reversibly using a low-power focused laser, while changing the environment from pure N_2 to air. This allows for the interlayer coupling to be precisely manipulated with submicron spatial resolution, facilitating site-programmable 2D light-emitting pixels whose emission intensity could be precisely varied by a factor exceeding 200×. Our results show that these atomically thin 2D heterostructures may be excellent candidates for oxygen sensing.

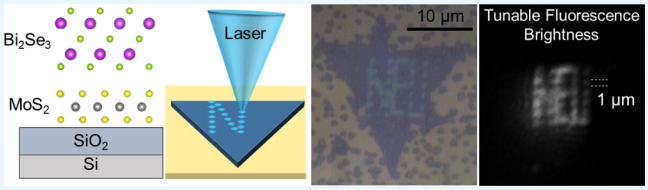

KEYWORDS: *transition metal dichalcogenides, bismuth selenide, 2D materials, interlayer coupling, intercalation*

INTRODUCTION

Two-dimensional (2D) heterostructures continue to draw enormous interest in view of their potential to advance both fundamental and applications-oriented research. They have contributed to fields as diverse as transistors,[1,2] optoelectronics,[3,4] information storage,[5,6] plasmonics,[7,8] photocatalysis,[9] capacitors,[10] biosensors,[11] spintronics,[12] high-density lithium storage with ultrafast diffusion,[13,14] and superconductivity.[15,16] The far-reaching success of 2D heterostructures is in part due to the large spectrum of properties. The properties of 2D heterostructures are more than a sum of the parent 2D materials, but are also a product of the interlayer interaction, which can be manipulated to engineer new capabilities. It has been shown that the twist angle,[17] interlayer spacing,[16] thermal annealing,[18,19] and intercalation of molecules[20−22] all influence the interlayer coupling strength. There are no tools to directly probe the interlayer coupling strength; however, its impact can be inferred by the extent it influences the properties. In this paper, we demonstrate that the interlayer coupling in Bi_2Se_3/MoS_2 2D heterostructures can be tuned by regulating the oxygen presence in the atmosphere, while applying controlled laser or thermal energy doses. The coupling strength is inferred using changes in the photoluminescence (PL) intensity, where lower PL corresponds to higher coupling. Our data suggest that the interlayer coupling is modulated by diffusively intercalating and deintercalating oxygen molecules.

The interlayer coupling in 2D materials is considered a promising parameter for designing materials with tailored properties; however, despite the significant interest, the interlayer coupling is not well understood, which is in part due to the lack of experimental techniques with the ability to precisely manipulate it. Some previous experimental work has focused on using global thermal annealing to manipulate the coupling; however, this method has not demonstrated precision and often requires several hours to complete.[18,19] Ion irradiation,[23] in-plane strain,[24] and lateral pressure[16,25] have all been shown to increase the interlayer coupling by

Received: February 15, 2019
Accepted: April 8, 2019
Published: April 8, 2019

DOI: 10.1021/acsami.9b02929
ACS Appl. Mater. Interfaces 2019, 11, 15913−15921

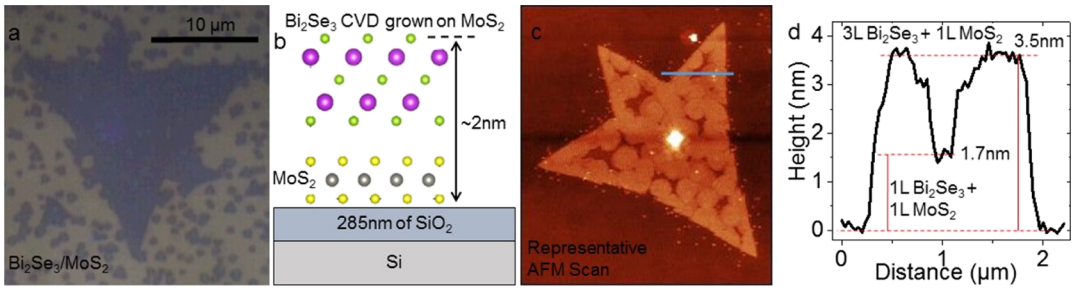

Figure 1. As-grown Bi_2Se_3/MoS_2 vertical 2D heterostructures. (a) Optical image of a Bi_2Se_3/MoS_2 vertical 2D heterostructure, where one layer of Bi_2Se_3 was uniformly grown on a monolayer MoS_2 crystal using vapor-phase deposition. (b) Side-view diagram of the heterostructure. (c) Representative AFM scan of a Bi_2Se_3/MoS_2 2D heterostructure and (d) corresponding line profile, demonstrating the uniform growth of the monolayer Bi_2Se_3 (with trilayer islands) across the entire MoS_2 crystal.

decreasing the interlayer separation; however, ion irradiation has also been shown to damage 2D materials and induce defects,[26] and applying strain or pressure alters the 2D material's lattice parameters and properties,[27] thereby introducing uncertainty. Work to manipulate the interlayer coupling via electric fields has only been theoretical, and follow-up experimental work is needed to confirm it.[28] In this paper, we demonstrate a facile method to tune the interlayer coupling in situ with high spatial resolution, all using ambient conditions and tools commonly found in a 2D research laboratory.

Monolayer MoS_2 is known, among other things, for having a bright PL because of the formation of tightly-bound excitons.[29] However, when only one layer of Bi_2Se_3 is grown on the monolayer MoS_2 using vapor-phase deposition, the bright PL is >99% quenched because the interlayer coupling induces a non-radiative exciton recombination pathway.[5] In this paper, we demonstrate that the PL can be controllably increased and decreased at small increments of only a few percent, suggesting that the coupling is being diminished or strengthened, respectively, at the same small increments. This is done by applying energy to the material in either an oxygen-present or oxygen-absent environment, which we believe facilitates the diffusive intercalation or deintercalation of oxygen molecules. Our results suggest that the diffusive intercalation of oxygen molecules induces the monolayer MoS_2 to behave more electronically independent, thereby restoring the radiative recombination pathway and facilitating the emergence of the signature PL peak.

The intercalation of molecules between layers has been shown to disrupt their coupling, leading to change in the properties.[13,20−22,30−36] For example, it has been shown that when several layer MoS_2 is intercalated with lithium or quaternary ammonium molecules, the signature monolayer PL emerges, suggesting that the intercalated molecules induce the MoS_2 layers to behave electronically independent, as if they were monolayers.[20,30,37] It has also been shown that oxygen can easily intercalate between 2D crystals and their substrates, decoupling the two materials and inducing them to behave more "freestanding" (i.e., electronically independent).[21,22,31−35]

A natural question arises as to why oxygen, vice other molecules in the atmosphere, manipulates the interlayer coupling in the Bi_2Se_3/MoS_2 2D heterostructure. Bi_2Se_3 is well-known for its oxygen affinity, where even trace amounts of oxygen dramatically affect its exotic topological properties.[38] Not only can oxygen react with Bi_2Se_3 to form a native oxide and new bonding,[39,40] but it has even been shown that oxygen is able to passively diffuse through multiple layers of Bi_2Se_3.[41] The interaction of Bi_2Se_3 and oxygen is complex and has been well-studied. A thorough literature review and how previous work relates to our findings are provided in Section S8.

RESULTS AND DISCUSSION

In this work, we obtain highly controllable, largely reversible, and site-selectable switching between direct (i.e., radiative and photoluminescence) and indirect (i.e., non-radiative) exciton recombination pathways in Bi_2Se_3/MoS_2 2D heterostructures (1−3 layers of Bi_2Se_3 grown on the monolayer MoS_2). Our approach allows permanent, in situ, electrodeless, and use-specific programming of the interlayer coupling and PL intensity. Exciton recombination dynamics could be switched (between radiative and non-radiative) by thermally treating the heterostructures in oxygen-present (e.g., air) versus inert atmospheres (i.e., Ar or N_2). Alternately, the switching could be localized in a highly controllable manner at ambient temperatures using a continuous wave 488 nm laser (as before, in air or under N_2), which allowed site-selective largely reversible manipulation of different regions of the same 2D heterostructures. Additionally, our results suggest that these 2D heterostructures might have applications as standard temperature−pressure high-density oxygen storage devices, potentially storing 69 kg/m^3 (a factor of 52 times the density of O_2 gas at 1 atm).

Figure 1a shows an optical image of Bi_2Se_3/MoS_2 2D heterostructures (1 layer MoS_2 + 1 layer Bi_2Se_3) on SiO_2, where the monolayer MoS_2 was grown using vapor-phase chalcogenization (VPC)[42] and Bi_2Se_3 was grown on top using vapor-phase deposition. Figure 1b is a side-view diagram of a typical Bi_2Se_3/MoS_2 2D heterostructure. Despite the huge lattice mismatch (e.g., 2.74−3.57 Å, see Figure S1), uniform layers of Bi_2Se_3 grow with high regularity on top of the MoS_2 crystal, suggesting strong van der Waals epitaxy-mediated growth between the two component layers.[43] Figure S2 shows the transfer characteristics of back-gated monolayer MoS_2 and Bi_2Se_3/MoS_2 field-effect transistor (FET) devices. The right shift of the threshold gate voltage in the 2D heterostructure indicates a relative downshift of the effective Fermi level because of reduction of excess n-type carriers (by about ~9.50 × 10^{12} cm^{-2}). The device response looks like neither monolayer MoS_2 nor few-layer Bi_2Se_3 (a semimetal),[44] suggesting that there is sufficient interlayer coupling to modify the electronic structure of both materials.

Figure 2a is an optical image of a Bi_2Se_3/MoS_2 vertical 2D heterostructure, where the energy was applied locally using a focused laser (168 μW for 8 min), while the sample was in an

DOI: 10.1021/acsami.9b02929
ACS Appl. Mater. Interfaces 2019, 11, 15913−15921

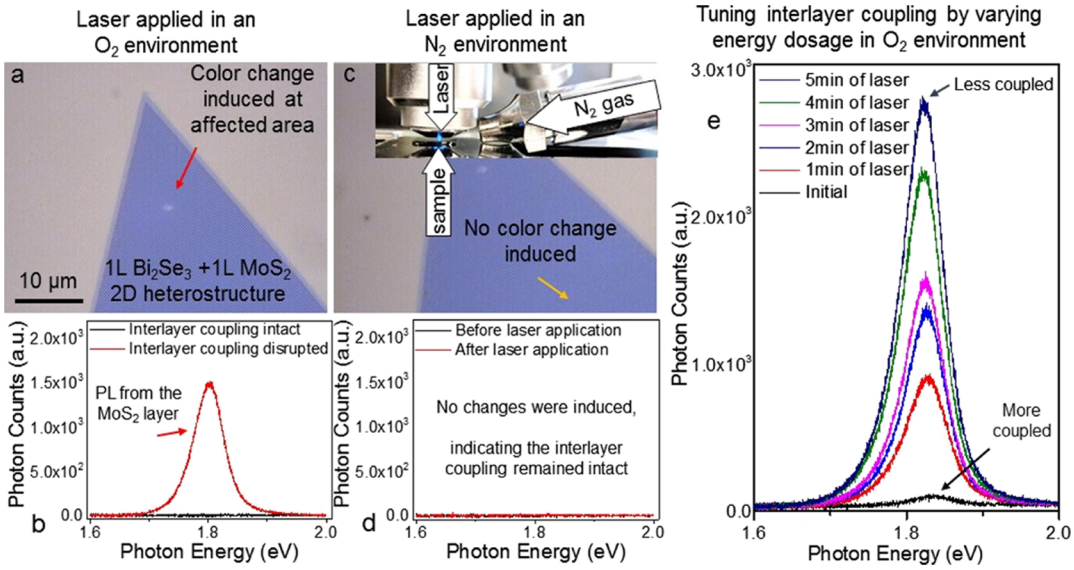

Figure 2. Manipulating the interlayer coupling using oxygen and energy. (a) Optical image of a Bi_2Se_3/MoS_2 vertical 2D heterostructure where energy was applied locally using a focused laser, while the sample was in an oxygen-present environment (i.e., air). The optical properties of the affected area were altered going from purple to white, allowing affected locations to be easily identified. (b) PL spectra from the same spot before and after energy was applied, demonstrating how the interlayer coupling can be manipulated. Initially, the PL spectra were flat; however, after applying a focused laser for 8 min at 168 μW, the PL spectra corresponding to the monolayer MoS_2 appeared, suggesting that the interlayer coupling was disrupted, allowing the MoS_2 layer to become more electronically independent. Electronically independent monolayer MoS_2 has a signature PL peak because of its tightly-bound excitons. (c) Laser was now applied to a different location (orange arrow) on the same sample at the same power (168 μW for 12 min), but the environment was changed from oxygen to nitrogen. Interestingly, the color change seen in (a) was not observed. The inset shows the setup where N_2 gas was flown across the sample to displace the oxygen. (d) PL spectra from the same spot before and after energy was applied show no perceivable appearance of PL, suggesting that the interlayer coupling was not affected. Thermal treatment experiments in Figure S4 demonstrate that applying heat in an oxygen environment disrupts the interlayer interaction and that the other components in air (e.g., N_2, H_2O, and CO_2) do not appear to affect the interlayer coupling. (e) PL spectra of a Bi_2Se_3/MoS_2 2D heterostructure before energy was applied, as well as after several consecutive doses, demonstrating how the PL intensity is dependent on the total dose.

oxygen-present environment (i.e., air). The red arrow identifies the affected location, which underwent a change in color from purple to white. Figure 2b shows its PL spectra before and after the energy dose was applied. Characteristic Bi_2Se_3/MoS_2 2D heterostructures do not have a PL, or only a very weak PL, because the interlayer coupling creates a non-radiative recombination path for the tightly-bound excitons that exist in the monolayer MoS_2.[5] However, if energy is applied to the heterostructure in the form of either thermal treatment or a laser, while the heterostructure is in an O_2-present environment, a PL spectrum emerges, which corresponds to that of monolayer MoS_2, suggesting that the interlayer coupling was disrupted and the signature MoS_2 excitons are recombined along radiative pathways. Further, Raman spectroscopy measurements show that the intensity of the monolayer MoS_2 modes increases after laser exposure in air, suggesting that the interlayer coupling has been diminished. Previous work has demonstrated a correlation between the intensity of the Raman modes and the interlayer coupling strength.[5,45−47] Atomic force microscopy (AFM) measurements demonstrate that Bi_2Se_3 remains on MoS_2 after a color change has been induced and the PL remerges, verifying that the change is not due simply to the removal of Bi_2Se_3 (Figure S3). A different spot on the same sample (Figure 2c, yellow arrow) was exposed to the same power (168 μW for 12 min), while being continuously purged with N_2 gas (inset Figure 2c), thereby removing oxygen from the vicinity of the exposed spot. We find that even with an increased laser dose (12 min vs 8 min exposure), there was neither a perceivable color change nor emergence of the PL peak (Figure 2d), suggesting that the interlayer coupling was not affected. Next, the atmosphere was switched back to air without changing the laser power or moving the sample—thereby reintroducing oxygen without changing the specific location being probed—resulting in a color change and a strong PL peak recovery (Figure S4b), confirming that oxygen plays a critical role in the observed changes. Detailed investigations in different gas environments in Figure S4 establish that oxygen (O_2), and not nitrogen, H_2O vapor, or carbon dioxide, is required to induce the changes and manipulate the interlayer coupling. Thermal treatment at 240 °C was able to modulate the interlayer coupling, suggesting that the mechanism is actuated when sufficient heat is present, and illumination with a particular wavelength is not required. Figure 2e demonstrates how the PL intensity is dependent on the energy dose applied, suggesting that the interlayer coupling can be manipulated in small increments. Later, in this paper, we demonstrate that the interlayer coupling can be tuned with high precision by controlling both the energy applied and the partial pressure of oxygen in the surrounding atmosphere.

Photoexcited e−h pairs in monolayered transition metal dichalcogenides (TMDs) form tightly-bound neutral and charged excitons.[29] In direct-gap monolayer TMDs, they recombine radiatively, producing well-known PL spectra. In few-layered and thicker TMDs, the quasiparticle band gaps are indirect; hence, the $K \rightarrow \Gamma$ indirect (non-radiative) recombination pathway becomes more favorable, resulting in progressively suppressed PL.[48] Indirect recombination in certain heterostructures can similarly be non-radiative, if the excitons formed near a $\vec{k}$-vector in the reciprocal lattice of one layer find the most favorable recombination pathway via a

DOI: 10.1021/acsami.9b02929
ACS Appl. Mater. Interfaces 2019, 11, 15913−15921

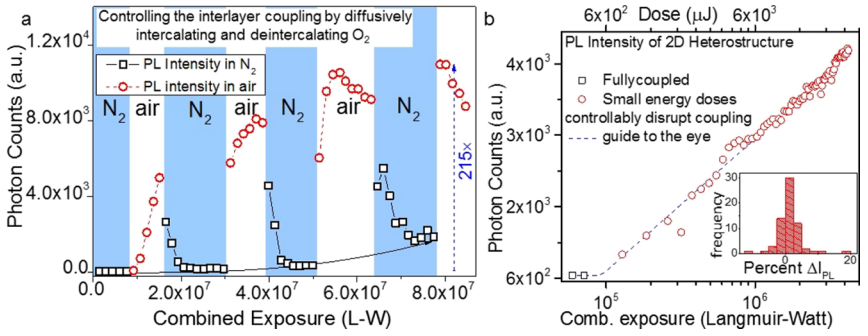

Figure 3. Tuning the interlayer coupling and PL intensity. (a) Variation of PL intensity under alternating air and nitrogen environments while a focused laser (i.e., energy) is applied, demonstrating that a nitrogen environment is able to restore the interlayer coupling. The solid black arrow shows how the baseline PL reading monotonically grows after repeated environment cycling and the PL's rate of change varies, suggesting that the 2D heterostructure may not return to its initial (as-grown) state. The dashed blue arrow shows the overall PL intensity growth factor, up to 215×, achievable by this cycling approach. (b) Correlation between laser (i.e., energy) exposure (in air) and the resulting PL intensity of a Bi_2Se_3/MoS_2 2D heterostructure using a calibrated recipe (50 μW, 6 s doses, followed by 1 μW, 60 s for collecting data), demonstrating a controlled disruption of interlayer coupling. Under this dose recipe, the radiative recombination was found to grow approximately logarithmically, and a vast majority of exposures result in a <5% change in intensity (see the inset). See also Figure S5 for other possible behaviors when the recipe is changed. Inset: Histogram of the change steps under each exposure. Both (a) and (b) taken together demonstrate an unprecedented degree of controlled manipulation of the interlayer coupling and PL achievable. Later, we demonstrate that this is possible in a site-selectable manner as well.

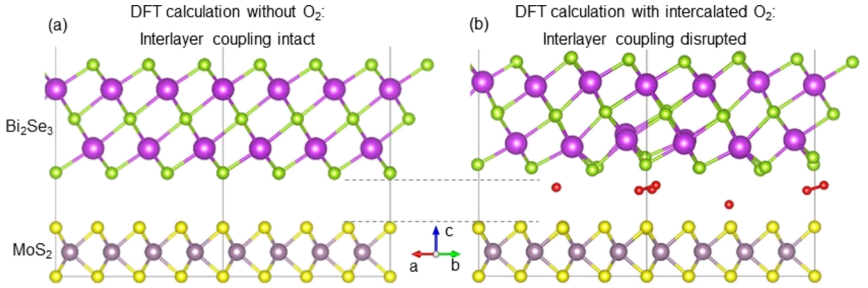

Figure 4. DFT calculations predict that intercalated O_2 diminishes the interlayer coupling. (a) DFT calculations of a rotationally aligned (i.e., twist angle is 0°) Bi_2Se_3/MoS_2 superlattice predict significant charge redistribution into the interlayer region and an influential interlayer coupling. (b) However, when O_2 molecules are placed in the interface between the layers, DFT calculations predict that the average interlayer separation increases from 3.57 to 4.18 Å (17% increase), diminishing the interlayer coupling. These results are in agreement with previous studies where intercalated O_2 between a 2D material and the substrate induces the 2D material to behave electronically independent (i.e., "freestanding"). Further, intercalation and deintercalation are diffusion-dependent processes, offering an explanation as to why the PL intensity rises and falls so quickly as the environment changes (Figure 3). DFT calculations predict an interlayer separation ~4.7 times larger than the diameter of an oxygen atom, suggesting that sufficient space exists for O_2 molecules to reside.

lower-energy state that is located at a different $\vec{k}$-point in the reciprocal lattice of the second layer. In all the as-grown Bi_2Se_3/MoS_2 2D heterostructures, the PL spectra were strongly quenched, suggesting that the interlayer coupling induced non-radiative recombination pathways for the excitons. Upon application of energy (either heat or laser) in an oxygen-present environment, all heterostructures recovered their radiative recombination pathways, suggesting that the interlayer coupling was disrupted, thereby inducing the MoS_2 layer to behave more electronically independent. Next, we show that the PL can be quenched again by applying energy (via either thermal treatment or laser exposure) in an O_2-free environment (Figure S4), demonstrating that the effects could be largely reversed and the interlayer coupling could be restored.

Remarkably, not only are we able to disrupt the interlayer coupling and increase the PL intensity, but we can also restore the interlayer coupling and decrease the PL intensity, which we believe is due to the intercalation and deintercalation of oxygen. Figure 3a shows the change in PL intensity of a Bi_2Se_3/MoS_2 2D heterostructure that is oxygenated and deoxygenated several cycles by switching the ambient atmosphere between air and nitrogen. This controllable switching of radiative and non-radiative exciton recombination pathways demonstrates the ability to both disrupt and restore the interlayer coupling. This process can be cycled several times, underscoring the fact that at the initial stage, under identical laser power, the oxygenation is reversed by the mere removal of the O_2 partial pressure in the ambient. This indicates that at least initially, the oxygenation process is diffusive and does not form chemical bonds. After a few cycles, the maximum PL intensity grows by as much as 215× and stops quenching fully, suggesting that other more permanent changes occur at higher energy dosage that possibly includes the formation of chemical bonds, trapped oxygen at edge sites, or new materials. These more permanent changes are less easily reversed and are in agreement with the monotonic growth of the baseline PL as the dose increases (discussed later in the paper and in Figure S4).

Figure 3b shows the variation of PL intensity measured after repeated doses (t = 6 s) of combined exposure to air (at ambient pressure) and laser power (at 50 μW). At this dose value, the PL was found to grow approximately logarithmically with combined exposure (along with incident energy), suggesting that the interlayer coupling can be tuned with

DOI: 10.1021/acsami.9b02929
ACS Appl. Mater. Interfaces 2019, 11, 15913−15921

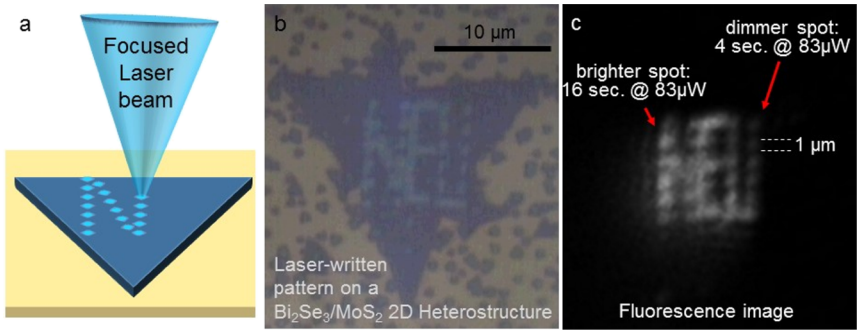

Figure 5. Site-selective manipulation of interlayer coupling and photoluminescence. (a) Schematic of a method to write patterns with site-selected interlayer coupling strength on Bi_2Se_3/MoS_2 2D heterostructures using a focused laser. (b) Optical image of a laser-written pattern on a Bi_2Se_3/MoS_2 2D heterostructure. The letters "NEU" were "drawn" using different exposure times. (c) Fluorescence microscopy image of the same sample (excitation λ = 488 nm). We note that using a focused laser beam, excitons of selected regions could be programmed to recombine radiatively (bright regions) or non-radiatively (dark regions), where the size of the affected area is dependent on the laser spot geometry and recipe used (i.e., the power and exposure duration). The smallest "radiative" regions were below a micron in diameter. This method allows for the rapid manipulation and measurement of the interlayer coupling with high spatial resolution, facilitating experiments that produce statistically significant results.

high precision. The logarithmic shape is in agreement with Fick's law of diffusion, which states that the diffusion flux will decrease as the system reaches equilibrium and whose general solution has an exponential form. Additionally, Fick's law has been used to describe the intercalation process, including the intercalation of lithium into vertically stacked bilayer graphene.[14] The inset shows that the intensity change (ΔI_{PL}) can be as low as ~5%, suggesting possible applications as low-cost atomically thin laser calorimeters or photon counters. Figure S5 demonstrates other possible behaviors when the recipe is changed.

The rapid changes observed in Figure 3 by simply switching the environment between air (i.e., O_2-present) and nitrogen (i.e., O_2-absent) suggest that oxygen diffuses in and out of the 2D heterostructure. As seen in Figure 4, the O_2 molecule is relatively small compared to the interlayer spacing. Further, it has been shown that O_2 molecules are able to permeate into Bi_2Se_3, demonstrating that they are able to fit between the atoms.[39−41] Density functional theory (DFT) calculations predict that the interlayer coupling in a Bi_2Se_3/MoS_2 2D heterostructure induces significant charge redistribution in the interlayer region, hybridizing nearest-neighbor atoms to form bonds, and that it is influential in modifying the bandstructure.[5] Interestingly, when O_2 molecules are placed in the interlayer region, DFT calculations predict that the materials will begin to separate, diminishing the interlayer coupling and inducing the layers to behave more electronically independent. It can be seen in Figure 4 that the interlayer spacing increases on average by 17% when five O_2 molecules are intercalated. Together, these results hint at the interesting possibility that these atomically thin layers may be excellent candidates for oxygen storage devices, potentially storing 69 kg/m^3 (a factor of 52 times the density of O_2 gas at 1 atm).

Figure 5 demonstrates a low-cost method to rapidly and precisely manipulate the interlayer coupling of Bi_2Se_3/MoS_2 2D heterostructures with submicron spatial resolution. Figure 5a is a schematic showing how a focused laser beam can be used to apply calibrated energy doses to precisely manipulate the interlayer coupling with high (submicron) spatial resolution. Figure 5b shows the optical image where the method in Figure 5a was used to trace the letters "NEU" using different exposure times, demonstrating a facile method to manipulate the interlayer coupling. The laser-written sample was then imaged using a fluorescence microscope (Figure 5c, λ_{ex} = 488 nm), demonstrating the ability to rapidly measure the degree of interlayer coupling disruption. The ability to rapidly write and read patterns with varying interlayer coupling strength facilitates experiments that produce statistically significant results. The fluorescence image also demonstrates site-selective light emission with a spatial size close to that of the incident laser spot, enabling photoluminescent pixels (PLPs) tailored down to submicron diameters. These site-programmable, color-selectable, atomically thin, micron-scale PLPs (with effective volumes ~10^{-21} m^3) are attractive for optical and optoelectronic applications that require ultrasmall form factors.

We now discuss the various possible mechanisms that could lead to the observed phenomena. As mentioned earlier, we tested the effect of all the primary gaseous species present in air and found it to be limited to oxygen (Figure S4), suggesting that only oxygen is able to intercalate. While attempting to understand as to why oxygen would have such a dramatic effect, vice the other gases, we found a large body of literature that discusses the impact of oxygen on Bi_2Se_3 and other materials in its class (e.g., Bi_2Te_3), suggesting, under different circumstances, both diffusive behavior and bond-forming mechanisms.[38−41,49−52] In sharp contrast, we were unable to find any literature that demonstrates the evidence of absorption or chemical reaction with nitrogen, argon, or carbon dioxide, suggesting that these molecules are significantly less reactive/interactive with Bi_2Se_3. The collective body of work appears to indicate that the energetics facilitate these interactions with oxygen, vice the other gases. From this, we conclude that interaction of oxygen, mediated by the bismuth selenide layer, is the most likely manner the changes are initiated. Further, oxygen has been shown to easily intercalate between 2D crystals and their substrates, decoupling the two materials and inducing them to behave more "freestanding" (i.e., electronically independent).[21,22,31−35,47,53] Indeed, our DFT calculations of a Bi_2Se_3/MoS_2 2D heterostructure predict that intercalated O_2 molecules force the materials apart, enlarging the interlayer separation by 17%, thereby diminishing their interlayer hybridization (see Section S7). This is further supported by our Raman measurements, which show that laser exposure in air increases the intensity of the monolayer MoS_2 modes (Figure S6). Previous work has shown that the

DOI: 10.1021/acsami.9b02929
ACS Appl. Mater. Interfaces 2019, 11, 15913−15921

intercalation of oxygen can diminish the interlayer coupling and modify the Raman modes.[47] Furthermore, intercalation is a diffusive process that has been shown to be reversible,[21,33−35] which could explain why laser exposure in an O_2-free environment is able to rapidly reverse the changes. Most notably, though, despite the large change in the observed return of the MoS_2 PL, the Raman peaks for both bismuth selenide and molybdenum disulfide are near-identically retained before and after the laser treatment, suggesting very little structural, electronic, or chemical changes to each of these layers individually. For this reason, physical separation of the two layers due to diffusion of oxygen into the interlayer region appears to be a very reasonable underlying mechanism.

If in fact oxygen diffuses into the interlayer, what path(s) does it take? A number of previous works have explored the intercalation of atoms in micron-scale graphene and other 2D materials, where it has been shown to be highly dependent on the number of grain boundaries.[13,14,21,22,34,35,54−59] More specifically, a single grain boundary of these systems was sufficient to enable large-scale intercalation in micron-scale samples, strongly suggesting that a high concentration of edges/grain boundaries under the laser spot might not be needed for the observed rapid intercalation/deintercalation. Bi_2Se_3 becomes highly crystalline on the underlying MoS_2, and when the 2D heterostructure is then exposed to a laser in air, Bi_2Se_3 becomes polycrystalline (Figure S1), suggesting the formation of grain boundaries. Together, these results suggest that (1) intercalation via grain boundaries is well-known and does not necessarily require a high density of grain boundaries to produce observable effects and (2) these intercalations result in a decoupling of the parent layers electronically. Although it does not provide direct evidence that intercalation of oxygen is taking place, in our case, these are strong indicators of the most possible mechanism (see Section S7 for a more detailed explanation).

Other possibilities include the formation of chemical bonds, trapped oxygen at edge sites, or new materials, possible explanations for the monotonic growth of the baseline PL intensity in Figure 3a. However, these are less likely in the initial stages of our experiments. It is well-established that Bi_2Se_3 is sensitive to oxygen, including the partial pressure of oxygen in air.[38−40,49−51] Studies have also shown that oxygen interacting with Bi_2Se_3 can form a native oxide layer. It is unlikely that native oxide growth is the primary mechanism, at least initially, because of the rapid rate of change and the easy reversibility of PL. We see quite easily that the oxygen insertion and release could be achieved (keeping all other parameters constant) by simply changing the partial pressure of oxygen in the surrounding environment. Additionally, while previous studies measured topographical changes because of the native oxide growth in Bi_2Se_3,[39] we found no such height changes (Figure S3). Oxidation of Bi_2Se_3 has also been shown to reveal new Raman spectral peaks.[60−62] In contrast, our Raman spectroscopic measurements show no new peaks (Figure S6). These, taken together with the oxygenation/release time scales, point more strongly in favor of a diffusive mechanism. Further, the logarithmic behavior when low powers are applied (Figure 3b) is in agreement with Fick's law of diffusion, which also has a logarithmic shape.

CONCLUSIONS

In conclusion, the interlayer coupling in vertically stacked 2D materials has demonstrated the ability to dramatically alter their properties and is considered a promising parameter for designing materials with tailored capabilities. The Bi_2Se_3/MoS_2 2D heterostructure is an ideal platform to study the interlayer interaction of 2D materials because it offers the ability to tune the interlayer coupling in situ and with high spatial resolution. From a fundamental perspective, in addition to rich excitonic physics, this system interplays strong spin−orbit coupling in noncentrosymmetric crystal structures and hence could potentially demonstrate novel correlated, spin and valley physics.[63,64] In addition, as site-programmable, color-selectable, atomically thin, micron-scale, and intensity-tunable PLPs, this system could be attractive for ultrathin and flexible optical information storage devices, color converters, microcavity lasers, and other photonic, plasmonic, and optoelectronic applications.[65,66] The strong oxygen selectivity of these heterostructures could also be potentially used as low-cost oxygen sensors and photon/power meters. We also showed data that suggested that these materials could be used as O_2 storage devices, potentially storing 69 kg/m^3 (a factor of 52 times the density of O_2 gas at 1 atm).

METHODS

Growth of Monolayer MoS_2 Crystals. Monolayer MoS_2 was grown using chemical vapor deposition (CVD).[42] The growth setup consisted of quartz tubes [1 in. (2.54 cm) in diameter] in a horizontal tube furnace (Lindberg/Blue M). A quartz boat, containing a thin layer of MoO_2 powder (3 mg) with SiO_2/Si (MTI Corporation) substrates suspended over the powder with the growth side facing down, was placed in the hot center of the furnace. Sulfur powder (150 mg) was placed near the insulating edge of the furnace upstream. The setup was pumped down and purged with argon gas before it was filled with an Ar atmosphere. Downstream was then opened to atmosphere, in addition to a constant 200 SCCM Ar flow. The furnace was heated to different temperatures and at variable rates, depending on the growth of the material. The growth was conducted in two stages, first stage and second stage, where the second stage would start once the first-stage temperature was reached. See the below table for material-specific growth information. After the elapsed time, the furnace was opened and allowed to cool rapidly (Table 1).

Table 1. Parameters for Growing Monolayer MoS_2 Using VPC

2D crystal	1st rate (°C/min)	1st temp (°C)	2nd rate (°C/min)	2nd temp (°C)	hold time (min)
MoS_2	50	500	5	712	20

Bi_2Se_3 growth was performed in an identical CVD setup, except a heating wrap was coiled around the quartz tube at the downstream end, leaving no gap between the furnace and the heating wrap. The Bi_2Se_3 powder (50 mg) was placed in the hot center of the furnace. The monolayer MoS_2 substrate was placed downstream ∼0.75 cm from the boundary between the furnace and the heating wrap. The system was pumped down to a base pressure of ∼10 mTorr before a 35-SCCM Ar flow was introduced, raising the growth pressure to ∼490 mTorr. The heating wrap was set to a temperature of 245 °C, and a temperature controller (J-KEM Scientific Model Apollo) ensured it remained within ±2 °C. The furnace was heated at a rate of 50 °C/min to 530 °C and then held there for 20−25 min depending on the desired thickness. Once growth was completed, the furnace was opened and the temperature controller was de-energized, allowing the setup to cool rapidly.

Thermal Treatment Experiments. All thermal treatment experiments were performed between 240 and 245 °C for 3 h. All experiments used a flow rate of 3 SCCM, except the thermal treatment under air, where no flow rate was used. The five environments were pure Ar, pure N_2, N_2 + H_2O^{vapor}, dry air (21%

DOI: 10.1021/acsami.9b02929
ACS Appl. Mater. Interfaces 2019, 11, 15913−15921

O_2 and 79% N_2), and air. All setups, except N_2 + H_2O^{vapor}, were pumped down and filled with the respective gas prior to thermal treatment. The N_2 + H_2O^{vapor} environment was created by flowing N_2 at 3 SCCM, while several boats with deionized H_2O were present in the tube. The heating of the tube caused the H_2O to evaporate. The downstream side "rained" significantly during the entire thermal treatment process and H_2O was still present in most of the boats, verifying that sufficient H_2O^{vapor} was present throughout the thermal treatment process.

Device Fabrication. Bi_2Se_3/MoS_2 2D heterostructures grown on 285 nm Si/SiO_2 were transferred to an identical chip, which had titanium/gold markers, by the poly(methyl methacrylate) (PMMA) transfer method. First, PMMA C4 was spin-coated at 4000 rpm for 60 s and baked 180 C for 1:30 min. Then the chip was immersed in 1 M KOH solution for 4 h. The obtained PMMA and the heterostructure film were transferred to a new substrate. This was followed by acetone and isopropyl alcohol (IPA) cleaning to remove PMMA residues.

FET devices were made on a 285 nm Si/SiO_2 substrate by E-beam lithography using PMMA C4 or A4. The electrodes (5 nm Ti/50 nm Au) were deposited by an e-beam evaporator with rate deposition 1 and 3 Å/s, respectively. The lift-off process was performed with acetone, followed by IPA cleaning.

Instrumentation. Raman and PL spectra were measured using a Renishaw Raman microscope equipped with a continuous wave 488 nm laser and a grating of 1800 lines/mm. A ×100 or ×150 objective focused the laser to diffraction-limited spot size. Transmission electron microscopy (TEM) images and selected area electron diffraction (SAED) patterns were collected from a JEOL 2010F operated at 200 kV. AFM images were taken with a NanoMagnetics Instruments Ambient AFM. All Raman, PL, AFM, and UV−vis experiments were performed under ambient condition.

COMPUTATIONAL DETAILS

Ab initio calculations were carried out by using the pseudopotential projector augmented-wave method[67] implemented in the Vienna ab initio simulation package[68] with an energy cutoff of 420 eV for the plane-wave basis set. Exchange−correlation effects were treated using the generalized gradient approximation,[69] and van der Waals corrections were included using the DFT-D2 method of Grimme,[70] where a 7 × 7 × 1 Γ-centered *k*-point mesh was used to sample the Brillouin zone. A large enough vacuum of 15 Å in the *z*-direction was used to ensure negligible interaction between the periodic images of the films. All the structures were relaxed using a conjugate gradient algorithm with an atomic force tolerance of 0.05 eV/Å and a total energy tolerance of 10^{-4} eV. The spin−orbit coupling effects were included in a self-consistent manner.

ASSOCIATED CONTENT

Supporting Information

The Supporting Information is available free of charge on the ACS Publications website at DOI: 10.1021/acsami.9b02929.

TEM SAED images, representative device data: monolayer MoS_2 versus Bi_2Se_3/MoS_2 2D heterostructure, AFM measurements, thermal treatment and laser exposure results, effect of laser exposure recipe, Raman modes: pre- and postlaser exposure, possible exciton recombination pathways, and discussion on interaction of Bi_2Se_3 with oxygen (PDF)

AUTHOR INFORMATION

Corresponding Author

*E-mail: s.kar@northeastern.edu.

ORCID

Zachariah Hennighausen: 0000-0001-5663-3331
Christopher Lane: 0000-0003-2945-9352
Jeremy T. Robinson: 0000-0001-8702-2680

Notes

The authors declare no competing financial interest.

ACKNOWLEDGMENTS

Support for this research was received from the National Science Foundation through grant numbers NSF ECCS 1351424 (a Northeastern University Provost's Tier-1 Seed Grant) and NSF CHE-1764221, as well as the U.S. Department of Veterans Affairs through the Post-9/11 GI Bill. The work at Northeastern University was supported by the US Department of Energy (DOE), Office of Science, Basic Energy Sciences grant number DE-FG02-07ER46352 (core research), and benefited from Northeastern University's Advanced Scientific Computation Center (ASCC), the NERSC supercomputing center through DOE grant number DE-AC02-05CH11231, and support (testing efficacy of advanced functionals in complex materials) from the DOE EFRC: Center for Complex Materials from First Principles (CCM) under DE-SC0012575.

REFERENCES

(1) Britnell, L.; Gorbachev, R. V.; Jalil, R.; Belle, B. D.; Schedin, F.; Mishchenko, A.; Georgiou, T.; Katsnelson, M. I.; Eaves, L.; Morozov, S. V.; et al. Field-Effect Tunneling Transistor Based on Vertical Graphene Heterostructures. *Science* **2012**, *335*, 947−950.

(2) Yu, W. J.; Li, Z.; Zhou, H.; Chen, Y.; Wang, Y.; Huang, Y.; Duan, X. Vertically Stacked Multi-Heterostructures of Layered Materials for Logic Transistors and Complementary Inverters. *Nat. Mater.* **2013**, *12*, 246−252.

(3) Britnell, L.; Ribeiro, R. M.; Eckmann, A.; Jalil, R.; Belle, B. D.; Mishchenko, A.; Kim, Y. J.; Gorbachev, R. V.; Georgiou, T.; Morozov, S. V.; et al. Strong Light-Matter Interactions in Heterostructures of Atomically Thin Films. *Science* **2013**, *340*, 1311−1314.

(4) Yu, W. J.; Liu, Y.; Zhou, H.; Yin, A.; Li, Z.; Huang, Y.; Duan, X. Highly Efficient Gate-Tunable Photocurrent Generation in Vertical Heterostructures of Layered Materials. *Nat. Nanotechnol.* **2013**, *8*, 952−958.

(5) Vargas, A.; Liu, F.; Lane, C.; Rubin, D.; Bilgin, I.; Hennighausen, Z.; DeCapua, M.; Bansil, A.; Kar, S. Tunable and laser-reconfigurable 2D heterocrystals obtained by epitaxial stacking of crystallographically incommensurate Bi 2 Se 3 and MoS 2 atomic layers. *Sci. Adv.* **2017**, *3*, No. e1601741.

(6) Bertolazzi, S.; Krasnozhon, D.; Kis, A. Nonvolatile Memory Cells Based on MoS2/Graphene Heterostructures. *ACS Nano* **2013**, *7*, 3246−3252.

(7) Agarwal, A.; Vitiello, M. S.; Viti, L.; Cupolillo, A.; Politano, A. Plasmonics with Two-Dimensional Semiconductors: From Basic Research to Technological Applications. *Nanoscale* **2018**, *10*, 8938−8946.

(8) Wang, G.; Li, L.; Fan, W.; Wang, R.; Zhou, S.; Lü, J.-T.; Gan, L.; Zhai, T. Interlayer Coupling Induced Infrared Response in WS2 /MoS2 Heterostructures Enhanced by Surface Plasmon Resonance. *Adv. Funct. Mater.* **2018**, *28*, 1800339.

(9) Zhu, M.; Sun, Z.; Fujitsuka, M.; Majima, T. Z-Scheme Photocatalytic Water Splitting on a 2D Heterostructure of Black Phosphorus/Bismuth Vanadate Using Visible Light. *Angew. Chem., Int. Ed.* **2018**, *57*, 2160−2164.

(10) Peng, L.; Peng, X.; Liu, B.; Wu, C.; Xie, Y.; Yu, G. Ultrathin Two-Dimensional MnO2/Graphene Hybrid Nanostructures for High-Performance, Flexible Planar Supercapacitors. *Nano Lett.* **2013**, *13*, 2151−2157.

DOI: 10.1021/acsami.9b02929
ACS Appl. Mater. Interfaces 2019, 11, 15913−15921

(11) Loan, P. T. K.; Zhang, W.; Lin, C.-T.; Wei, K.-H.; Li, L.-J.; Chen, C.-H. Graphene/MoS2Heterostructures for Ultrasensitive Detection of DNA Hybridisation. *Adv. Mater.* **2014**, *26*, 4838−4844.
(12) Song, T.; Cai, X.; Tu, M. W.-Y.; Zhang, X.; Huang, B.; Wilson, N. P.; Seyler, K. L.; Zhu, L.; Taniguchi, T.; Watanabe, K.; et al. Giant Tunneling Magnetoresistance in Spin-Filter van Der Waals Heterostructures. *Science* **2018**, *360*, 1214.
(13) Kühne, M.; Börrnert, F.; Fecher, S.; Ghorbani-Asl, M.; Biskupek, J.; Samuelis, D.; Krasheninnikov, A. V.; Kaiser, U.; Smet, J. H. Reversible Superdense Ordering of Lithium between Two Graphene Sheets. *Nature* **2018**, *564*, 234.
(14) Kühne, M.; Paolucci, F.; Popovic, J.; Ostrovsky, P. M.; Maier, J.; Smet, J. H. Ultrafast Lithium Diffusion in Bilayer Graphene. *Nat. Nanotechnol.* **2017**, *12*, 895−900.
(15) Cao, Y.; Fatemi, V.; Fang, S.; Watanabe, K.; Taniguchi, T.; Kaxiras, E.; Jarillo-Herrero, P. Unconventional Superconductivity in Magic-Angle Graphene Superlattices. *Nature* **2018**, *556*, 43−50.
(16) Yankowitz, M.; Jung, J.; Laksono, E.; Leconte, N.; Chittari, B. L.; Watanabe, K.; Taniguchi, T.; Adam, S.; Graf, D.; Dean, C. R. Dynamic band-structure tuning of graphene moiré superlattices with pressure. *Nature* **2018**, *557*, 404.
(17) Hennighausen, Z.; Kar, S. Probing the Interlayer Interaction between Dissimilar 2D Heterostructures by In-Situ Rearrangement of Their Interface. *2D Mater* **2019**, DOI: 10.1088/2053-1583/ab136e.
(18) Alexeev, E. M.; Catanzaro, A.; Skrypka, O. V.; Nayak, P. K.; Ahn, S.; Pak, S.; Lee, J.; Sohn, J. I.; Novoselov, K. S.; Shin, H. S.; et al. Imaging of Interlayer Coupling in van Der Waals Heterostructures Using a Bright-Field Optical Microscope. *Nano Lett.* **2017**, *17*, 5342−5349.
(19) Wang, F.; Wang, J.; Guo, S.; Zhang, J.; Hu, Z.; Chu, J. Tuning Coupling Behavior of Stacked Heterostructures Based on MoS2, WS2 and WSe2. *Sci. Rep.* **2017**, *7*, 44712.
(20) Wang, C.; He, Q.; Halim, U.; Liu, Y.; Zhu, E.; Lin, Z.; Xiao, H.; Duan, X.; Feng, Z.; Cheng, R.; et al. Monolayer Atomic Crystal Molecular Superlattices. *Nature* **2018**, *555*, 231−236.
(21) Grånäs, E.; Knudsen, J.; Schröder, U. A.; Gerber, T.; Busse, C.; Arman, M. A.; Schulte, K.; Andersen, J. N.; Michely, T. Oxygen Intercalation under Graphene on Ir(111): Energetics, Kinetics, and the Role of Graphene Edges. *ACS Nano* **2012**, *6*, 9951−9963.
(22) Du, Y.; Zhuang, J.; Wang, J.; Li, Z.; Liu, H.; Zhao, J.; Xu, X.; Feng, H.; Chen, L.; Wu, K.; et al. Quasi-Freestanding Epitaxial Silicene on Ag(111) by Oxygen Intercalation. *Sci. Adv.* **2016**, *2*, No. e1600067.
(23) Tan, Y.; Liu, X.; He, Z.; Liu, Y.; Zhao, M.; Zhang, H.; Chen, F. Tuning of Interlayer Coupling in Large-Area Graphene/WSe2 van Der Waals Heterostructure via Ion Irradiation: Optical Evidences and Photonic Applications. *ACS Photonics* **2017**, *4*, 1531−1538.
(24) Pak, S.; Lee, J.; Lee, Y.-W.; Jang, A.-R.; Ahn, S.; Ma, K. Y.; Cho, Y.; Hong, J.; Lee, S.; Jeong, H. Y.; et al. Strain-Mediated Interlayer Coupling Effects on the Excitonic Behaviors in an Epitaxially Grown MoS2/WS2 van Der Waals Heterobilayer. *Nano Lett.* **2017**, *17*, 5634−5640.
(25) Fu, X.; Li, F.; Lin, J.-F.; Gong, Y.; Huang, X.; Huang, Y.; Gao, H.; Zhou, Q.; Cui, T. Coupling-Assisted Renormalization of Excitons and Vibrations in Compressed MoSe2-WSe2 Heterostructure. *J. Phys. Chem. C* **2018**, *122*, 5820−5828.
(26) Maguire, P.; Fox, D. S.; Zhou, Y.; Wang, Q.; O'Brien, M.; Jadwiszczak, J.; Cullen, C. P.; McManus, J.; Bateman, S.; McEvoy, N.; et al. Defect Sizing, Separation, and Substrate Effects in Ion-Irradiated Monolayer Two-Dimensional Materials. *Phys. Rev. B* **2018**, *98*, 134109.
(27) Roldán, R.; Castellanos-Gomez, A.; Cappelluti, E.; Guinea, F. Strain Engineering in Semiconducting Two-Dimensional Crystals. *J. Phys.: Condens. Matter* **2015**, *27*, 313201.
(28) Gao, S.; Yang, L.; Spataru, C. D. Interlayer Coupling and Gate-Tunable Excitons in Transition Metal Dichalcogenide Heterostructures. *Nano Lett.* **2017**, *17*, 7809−7813.
(29) Mak, K. F.; He, K.; Lee, C.; Lee, G. H.; Hone, J.; Heinz, T. F.; Shan, J. Tightly bound trions in monolayer MoS2. *Nat. Mater.* **2013**, *12*, 207−211.
(30) Wang, Y.; Ou, J. Z.; Balendhran, S.; Chrimes, A. F.; Mortazavi, M.; Yao, D. D.; Field, M. R.; Latham, K.; Bansal, V.; Friend, J. R.; et al. Electrochemical Control of Photoluminescence in Two-Dimensional MoS2 Nanoflakes. *ACS Nano* **2013**, *7*, 10083−10093.
(31) Ávarez-Fragar, L.; Rubio-Zuazo, J.; Jiménez-Villacorta, F.; Climent-Pascual, E.; Ramírez-Jiménez, R.; Prieto, C.; de Andrés, A. Oxidation Mechanisms of Copper under Graphene: The Role of Oxygen Encapsulation. *Chem. Mater.* **2017**, *29*, 3257−3264.
(32) Kowalski, G.; Tokarczyk, M.; Dąbrowski, P.; Ciepielewski, P.; Możdżonek, M.; Strupiński, W.; Baranowski, J. M. New X-ray insight into oxygen intercalation in epitaxial graphene grown on 4H-SiC(0001). *J. Appl. Phys.* **2015**, *117*, 105301.
(33) Sutter, P.; Sadowski, J. T.; Sutter, E. A. Chemistry under Cover: Tuning Metal−Graphene Interaction by Reactive Intercalation. *J. Am. Chem. Soc.* **2010**, *132*, 8175−8179.
(34) Ulstrup, S.; Lacovig, P.; Orlando, F.; Lizzit, D.; Bignardi, L.; Dalmiglio, M.; Bianchi, M.; Mazzola, F.; Baraldi, A.; Larciprete, R.; et al. Photoemission Investigation of Oxygen Intercalated Epitaxial Graphene on Ru(0001). *Surf. Sci.* **2018**, *678*, 57.
(35) Bignardi, L.; Lacovig, P.; Dalmiglio, M. M.; Orlando, F.; Ghafari, A.; Petaccia, L.; Baraldi, A.; Larciprete, R.; Lizzit, S. Key Role of Rotated Domains in Oxygen Intercalation at Graphene on Ni(1 1 1). *2D Mater* **2017**, *4*, 025106.
(36) Wan, J.; Lacey, S. D.; Dai, J.; Bao, W.; Fuhrer, M. S.; Hu, L. Tuning Two-Dimensional Nanomaterials by Intercalation: Materials, Properties and Applications. *Chem. Soc. Rev.* **2016**, *45*, 6742−6765.
(37) Xiong, F.; Wang, H.; Liu, X.; Sun, J.; Brongersma, M.; Pop, E.; Cui, Y. Li Intercalation in MoS2: In Situ Observation of Its Dynamics and Tuning Optical and Electrical Properties. *Nano Lett.* **2015**, *15*, 6777−6784.
(38) Chen, Y. L.; Chu, J. H.; Analytis, J. G.; Liu, Z. K.; Igarashi, K.; Kuo, H. H.; Qi, X. L.; Mo, S. K.; Moore, R. G.; Lu, D. H.; et al. Massive Dirac Fermion on the Surface of a Magnetically Doped Topological Insulator. *Science* **2010**, *329*, 659−662.
(39) Green, A. J.; Dey, S.; An, Y. Q.; O'Brien, B.; O'Mullane, S.; Thiel, B.; Diebold, A. C. Surface Oxidation of the Topological Insulator Bi2Se3. *J. Vac. Sci. Technol., A* **2016**, *34*, 061403.
(40) Kong, D.; Cha, J. J.; Lai, K.; Peng, H.; Analytis, J. G.; Meister, S.; Chen, Y.; Zhang, H.-J.; Fisher, I. R.; Shen, Z.-X.; et al. Rapid Surface Oxidation as a Source of Surface Degradation Factor for Bi2Se3. *ACS Nano* **2011**, *5*, 4698−4703.
(41) Bansal, N.; Kim, Y. S.; Edrey, E.; Brahlek, M.; Horibe, Y.; Iida, K.; Tanimura, M.; Li, G.-H.; Feng, T.; Lee, H.-D.; et al. Epitaxial Growth of Topological Insulator Bi2Se3 Film on Si(111) with Atomically Sharp Interface. *Thin Solid Films* **2011**, *520*, 224−229.
(42) Bilgin, I.; Liu, F.; Vargas, A.; Winchester, A.; Man, M. K. L.; Upmanyu, M.; Dani, K. M.; Gupta, G.; Talapatra, S.; Mohite, A. D.; et al. Chemical Vapor Deposition Synthesized Atomically Thin Molybdenum Disulfide with Optoelectronic-Grade Crystalline Quality. *ACS Nano* **2015**, *9*, 8822−8832.
(43) Walsh, L. A.; Hinkle, C. L. van der Waals epitaxy: 2D materials and topological insulators. *Appl. Mater. Today* **2017**, *9*, 504−515.
(44) Kim, D.; Syers, P.; Butch, N. P.; Paglione, J.; Fuhrer, M. S. Coherent topological transport on the surface of Bi2Se3. *Nat. Commun.* **2013**, *4*, 2040.
(45) Ding, L.; Ukhtary, M. S.; Chubarov, M.; Choudhury, T. H.; Zhang, F.; Yang, R.; Zhang, A.; Fan, J. A.; Terrones, M.; Redwing, J. M.; et al. Understanding Interlayer Coupling in TMD-HBN Heterostructure by Raman Spectroscopy. *IEEE Trans. Electron Devices* **2018**, *65*, 4059.
(46) Yan, Y.; Li, F.; Gong, Y.; Yao, M.; Huang, X.; Fu, X.; Han, B.; Zhou, Q.; Cui, T. Interlayer Coupling Affected Structural Stability in Ultrathin MoS2: An Investigation by High Pressure Raman Spectroscopy. *J. Phys. Chem. C* **2016**, *120*, 24992−24998.
(47) Oliveira, M. H.; Schumann, T.; Fromm, F.; Koch, R.; Ostler, M.; Ramsteiner, M.; Seyller, T.; Lopes, J. M. J.; Riechert, H.

Formation of High-Quality Quasi-Free-Standing Bilayer Graphene on SiC(0001) by Oxygen Intercalation upon Annealing in Air. *Carbon* **2013**, *52*, 83−89.
(48) Splendiani, A.; Sun, L.; Zhang, Y.; Li, T.; Kim, J.; Chim, C.-Y.; Galli, G.; Wang, F. Emerging Photoluminescence in Monolayer MoS2. *Nano Lett.* **2010**, *10*, 1271−1275.
(49) Wang, X.; Bian, G.; Miller, T.; Chiang, T.-C. Fragility of Surface States and Robustness of Topological Order in Bi2Se3 against Oxidation. *Phys. Rev. Lett.* **2012**, *108*, 096404.
(50) Yashina, L. V.; Sánchez-Barriga, J.; Scholz, M. R.; Volykhov, A. A.; Sirotina, A. P.; Neudachina, V. S.; Tamm, M. E.; Marchenko, D.; Springholz, G.; Bauer, G.; et al. Negligible Surface Reactivity of Topological Insulators Bi2Se3 and Bi2Te3 towards Oxygen and Water. *ACS Nano* **2013**, *7*, 5181−5191.
(51) Yeh, Y.-C.; Ho, P.-H.; Wen, C.-Y.; Shu, G.-J.; Sankar, R.; Chou, F.-C.; Chen, C.-W. Growth of the Bi2Se3 Surface Oxide for Metal-Semiconductor-Metal Device Applications. *J. Phys. Chem. C* **2016**, *120*, 3314−3318.
(52) Music, D.; Chang, K.; Schmidt, P.; Braun, F. N.; Heller, M.; Hermsen, S.; Pöllmann, P. J.; Schulzendorff, T.; Wagner, C. On atomic mechanisms governing the oxidation of Bi2Te3. *J. Phys.: Condens. Matter* **2017**, *29*, 485705.
(53) Romero-Muñiz, C.; Martín-Recio, A.; Pou, P.; Gómez-Rodríguez, J. M.; Pérez, R. Unveiling the atomistic mechanisms for oxygen intercalation in a strongly interacting graphene-metal interface. *Phys. Chem. Chem. Phys.* **2018**, *20*, 13370−13378.
(54) Ligato, N.; Caputi, L. S.; Cupolillo, A. Oxygen Intercalation at the Graphene/Ni(111) Interface: Evidences of Non-Metal Islands underneath Graphene Layer. *Carbon* **2016**, *100*, 258−264.
(55) Ma, L.; Zeng, X. C.; Wang, J. Oxygen Intercalation of Graphene on Transition Metal Substrate: An Edge-Limited Mechanism. *J. Phys. Chem. Lett.* **2015**, *6*, 4099−4105.
(56) Píš, I.; Nappini, S.; Bondino, F.; Menteş, T. O.; Sala, A.; Locatelli, A.; Magnano, E. Fe Intercalation under Graphene and Hexagonal Boron Nitride In-Plane Heterostructure on Pt(111). *Carbon* **2018**, *134*, 274−282.
(57) Zhang, H.; Fu, Q.; Cui, Y.; Tan, D.; Bao, X. Growth Mechanism of Graphene on Ru(0001) and O2 Adsorption on the Graphene/Ru(0001) Surface. *J. Phys. Chem. C* **2009**, *113*, 8296−8301.
(58) Kowalski, G.; Tokarczyk, M.; Dąbrowski, P.; Ciepielewski, P.; Możdżonek, M.; Strupiński, W.; Baranowski, J. M. New X-Ray Insight into Oxygen Intercalation in Epitaxial Graphene Grown on 4H-SiC(0001). *J. Appl. Phys.* **2015**, *117*, 105301.
(59) Li, T.; Yarmoff, J. A. Intercalation and Desorption of Oxygen between Graphene and Ru(0001) Studied with Helium Ion Scattering. *Phys. Rev. B* **2017**, *96*, 155441.
(60) Trentelman, K. A note on the characterization of bismuth black by Raman microspectroscopy. *J. Raman Spectrosc.* **2009**, *40*, 585−589.
(61) Hardcastle, F. D.; Wachs, I. E. The Molecular Structure of Bismuth Oxide by Raman Spectroscopy. *J. Solid State Chem.* **1992**, *97*, 319−331.
(62) Steele, J. A.; Lewis, R. A. In situ micro-Raman studies of laser-induced bismuth oxidation reveals metastability of β-Bi_2O_3 microislands. *Opt. Mater. Express* **2014**, *4*, 2133−2142.
(63) Hamamoto, K.; Ezawa, M.; Kim, K. W.; Morimoto, T.; Nagaosa, N. Nonlinear Spin Current Generation in Noncentrosymmetric Spin-Orbit Coupled Systems. *Phys. Rev. B* **2017**, *95*, 224430.
(64) Smidman, M.; Salamon, M. B.; Yuan, H. Q.; Agterberg, D. F. Superconductivity and spin-orbit coupling in non-centrosymmetric materials: a review. *Rep. Prog. Phys.* **2017**, *80*, 036501.
(65) Xiao, J.; Zhao, M.; Wang, Y.; Zhang, X. Excitons in Atomically Thin 2D Semiconductors and Their Applications. *Nanophotonics* **2017**, *6* (). DOI: DOI: 10.1515/nanoph-2016-0160.
(66) Ye, Y.; Wong, Z. J.; Lu, X.; Ni, X.; Zhu, H.; Chen, X.; Wang, Y.; Zhang, X. Monolayer Excitonic Laser. *Nat. Photonics* **2015**, *9*, 733−737.
(67) Kresse, G.; Joubert, D. From Ultrasoft Pseudopotentials to the Projector Augmented-Wave Method. *Phys. Rev. B: Condens. Matter Mater. Phys.* **1999**, *59*, 1758−1775.
(68) Kresse, G.; Furthmüller, J. Efficient iterative schemes forab initiototal-energy calculations using a plane-wave basis set. *Phys. Rev. B: Condens. Matter Mater. Phys.* **1996**, *54*, 11169−11186.
(69) Perdew, J. P.; Burke, K.; Ernzerhof, M. Generalized Gradient Approximation Made Simple. *Phys. Rev. Lett.* **1996**, *77*, 3865−3868.
(70) Grimme, S. Semiempirical GGA-type density functional constructed with a long-range dispersion correction. *J. Comput. Chem.* **2006**, *27*, 1787−1799.

DOI: 10.1021/acsami.9b02929
ACS Appl. Mater. Interfaces 2019, 11, 15913−15921